`Vol. 5, No. 3, pp. 372-395, (September 2024)
DOI: 10.21608/aujes.2024.299836.1258
Aswan University Journal of Environmental Studies (AUJES)
Online ISSN: 2735-4237, Print ISSN: 2735-4229
Journal homepage: https://aujes.journals.ekb.eg/ E-mail: AUJES@aswu.edu.eg
Original research

Mineralogical and geochemical aspects of garnet bearing S-type granite, Wadi Nugrus, South Eastern Desert, Egypt.

Gehan B. El Shaib[1], Abdelhady Radwan[2]

1.Nuclear Materials Authority, Egypt.
2.Geology department, Faculty of Science, Aswan University

Received: 27/6/2024 Accepted: 8/9/2024

Abstract:

The garnet bearing muscovite granite (GMG) of Gabal El Magal El Harami along Wadi Nugrus shear zone represents one of important rare metal bearing granites in the South Eastern Desert of Egypt. The Landsat-8 (OLI) remote sensing data, field works, and petrographic investigations revealed that the GMG is emplaced within old continental gneissic units, ophiolite mélange and island arc associations. It forms NNW–SSE trending elongate belt parallel to the famous Wadi Nugrus shear zone. It also appears as small off-shoot dyke-like bodies, huge semicircular mass with domal shape. It is essentially composed of plagioclase, K-feldspar, quartz, muscovite and garnet. This granite is enriched by some accessory minerals (i.e. garnet spessartine, zircon, fluorite, monazite, xenotime, apatite, iron) and rare metals (i.e. niobium - tantalum, wolframite, cassiterite, beryl). Moreover it is enriched in Ba, Rb, U, Th, K, Nb, but have low Sr, Y. The studied granite intrusion has S-type peraluminous signature and high K-calc alkaline affinity. This intrusion is highly fractionated granite that was formed during the post orogenic times through partial melting of metagraywackes from lower crustal sources under high temperature and pressure conditions.

Keywords: Garnetiferous granite, Wadi Nugrus, S-type granite, Gabal Magal El Harami

1. Introduction

The prominence of Neoproterozoic rocks association in the Egyptian Eastern Desert forms the drastic northern termination of the Nubian Shield, which was tangent with the Arabian Shield prior to the inauguration of the Red Sea. The Arabian-Nubian Shield (ANS) has been invaded by copious masses of granitoid rocks that have diverse geochemistry, ages, and tectonic settings (e.g., Ali et al., 2012; Moghazi et al., 2015; Basta et al., 2017; Emam et al., 2018 ; Lehmann et al., 2020; Emam and Radwan, 2021). The Egyptian granitoids rocks were categorized into two main categories, older or syntectectonic and younger or post-late granitoids. The former type ranges in their compositions between tonalite, diorite, quartz diorite to granodiorite emplaced during subduction regimes of the Pan African orogeny at 870 - 614 Ma (Hassan and Hashad, 1990; Stern, 1994; Kröner et al., 1994).

Corresponding author*: E-mail address: abdelhady_geoscience@aswu.edu.eg

The later types have a composition of monzogranite, syenogranites to alkali feldspar granites, and were formed during relaxation regimes at around 610 - 550 Ma (e.g., Stern, 1994; Moghazi, 1999; Lehmann et al., 2020). One of most remarkable features of the late-post tectonic granitic rocks is their enrichment by rare metals with economic grades (e.g., Moghazi et al., 2015; El Hadek et al., 2016; Abu El-Rus et al., 2017; Zoheir et al., 2020). Generally the rare metal bearing granites are classified into S and I- types. Breiter et al. (2020) explained the difference between the two rare metal bearing granite types based on alumina, titanium, lithium, posphrous, rubidium and tin that are exist in relatively higher values in S-type settings. Moreover, Al contents are higher than 450 ppm in S-affinity granites, while it is below 250 ppm in I-type.

The rock association of the Nugrus shear zone is a matter of discussion by several works (e.g., Gharib et al. 2011; Abu El-Atta et al. 2021; El Fakharani et al., 2021; Azer et al., 2024). In the Egyptian Eastern Desert, the tectonic boundary separating the Central part from Southern one is widely known as the Sha'it–Nugrus shear zone (Fowler and Osman, 2009). This zone is explained as thick area of highly sheared foliated associations separating the famous Migif-Hafafit gneissose units in the South from Central terrain. This boundary has NE trend that passes through Wadi Sha'it to Wadi Nugrus, and continued to the Gabal Sikait at the east till the red sea coast. The studied intrusion is located at wadi Nugrus Shear zone between latitude 34° 30' – 34° 40' E and longitude 24° 45' – 24° 56' N (Fig. 1). The present study presents detailed description of petrography, mineralogy and geochemistry of Gabal El Magal El Harami garnetiferous muscovite granite along Wadi Nugrus area, in order to infer the petrogenesis and tectonic environment of these rocks.

2- Materials and Methods

The different rock units occupying the studied area were firstly differentiated using Landsat-8 (OLI) data and evidenced by field and microscopic studies. The image processing operations were done using subsets of Landsat-8 (OLI) scene (ID: LC81730432016139LGN00, Path 173/Row 43, produced on May, 2016) that was downloaded from Earth Explorer web site (https://earthexplorer.usgs.gov/). The processing techniques were achieved using image processing and analysis software ENVI. 4.5. These techniques comprise false color composites (FCC), band ratios, minimum noise fraction (MNF), and principal component analysis (PCA).

For chemical analyses, twenty one granite samples were chemically investigated for their major and some trace elements. These granite samples were analyzed at the laboratories of the Egyptian Nuclear Materials Authority. The major oxides were analysed using fused pellets method, where the fused pellets were intended based on the method of Shapiro and Brannock (1962). The determination of most trace elements were done through using of pressed powder pellets. The investigated elements were carefully analysed using of X-ray fluorescence technique (Philips-PW 1480 X-ray spectrometer X-unique II with automatic sample changer PW 1510). The elements were standardized against known rate of international criterion utilizing the standards given by Govindaraju (1984). The Sc, Hf, Ta, Th and U elements were determined by using of instrumental neutron activation analysis (INAA). Absolute accuracy has been estimated via rapprochement with international reference values analyzed along with the samples and is generally less than 2%.

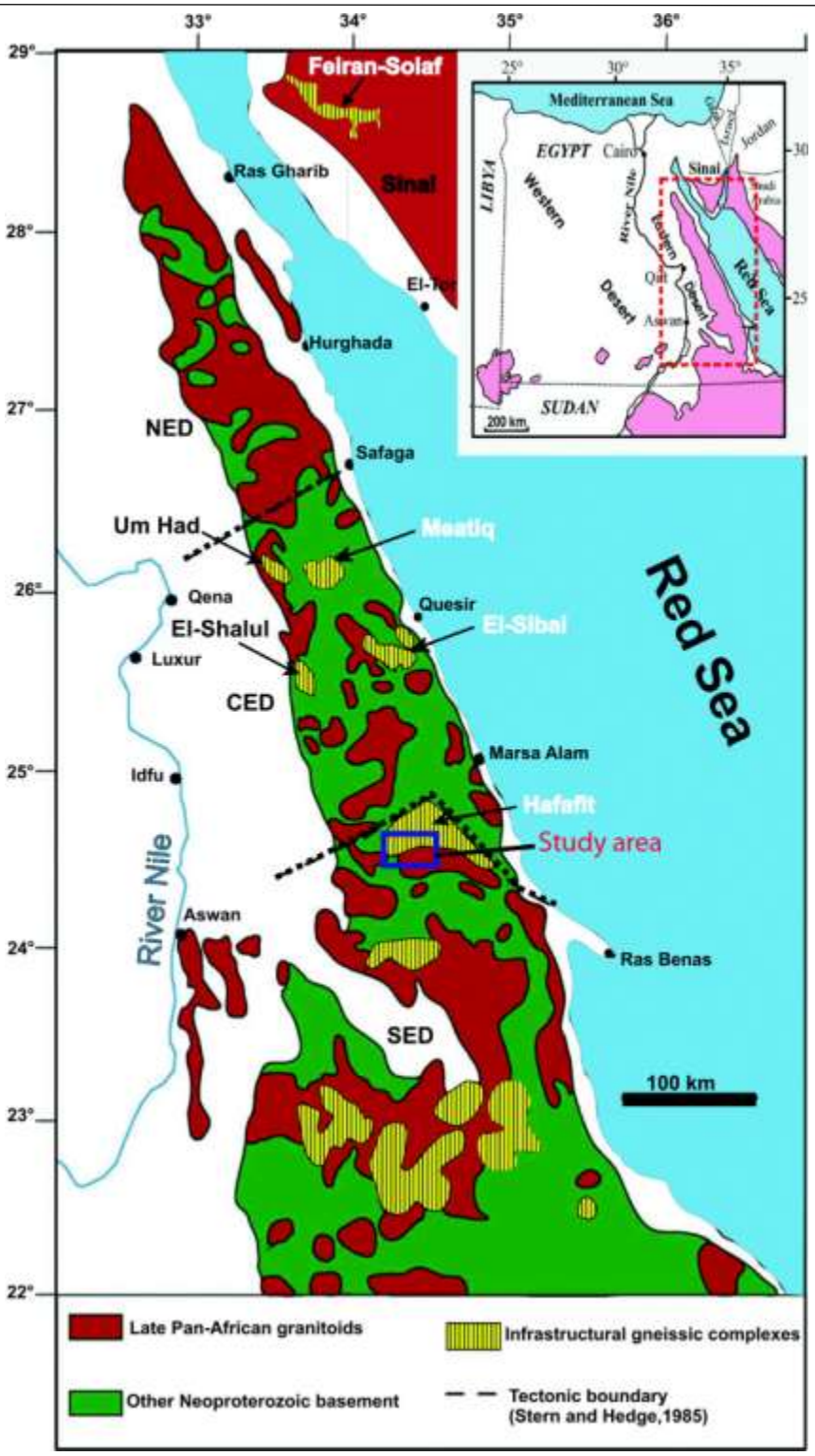

Fig. 1. Geologic map of the basement terrains of the Eastern Desert after Liégeois and Stern, (2010). The tectonic boundaries are after Stern and Hedge, (1985). The location of studied intrusion is shown by the blue rectangle. Geographic map showing the area of Arabian-Nubian Shield by red dashed rectangle.

For X-ray investigations, seven samples were taken from the mineralized and metasomatized zones of the GMG. These mineralized samples were crushed to 0.23 - 0.5mm in size then they were sieved into different mesh fractions. The resulted mesh size particles were concentrated to separate the heavy minerals. The concentration was done by using of wufly table which enables to remove the light mineral fractions. After few time the heavy fractions were dried. A hand magnet is used to separate iron rich phases, however the iron free phases are concentrated through using of bromoform (Sp. G. = 2.85). In order to isolate the different fractions of the heavy minerals, the Frantz Isodynamic Separator is used which can isolate the heavy fraction depending on their susceptibilities. This process was then followed by picking up of these phases using hand pick and binocular microscope. The picked materials were then investigated using the Scanning Electron Microscope [Model Phillips XL 30 with Energy Dispersive X-ray (EDX)] at laboratory of Egyptian Nuclear Materials Authority (NMA). The XRD patterns were acquired through using of Malvern Panalytical Empyrean X-ray diffractometer with CuKa radiation (λ=1.5418Ao) operating at a tube voltage of 40 $_{Kv}$ and 30 Ma. The resulted diffraction patterns were then listed in the extent between 5 and 75^{o} (2θ), and were correlated with existing referenced patterns in powder diffraction files (PDF).

3-Results and discussion

3.1. Geologic setting

Garnet bearing muscovite granite (GMG) forms elongate mass stretched in the NW-SE trend for about 10 km length and 5 Km width (Fig. 2). It form highly rugged topographic pluton with conspicuous peak. It is surrounded by high grade Hafafit gneissic dome and low-medium grade metamorphic suite of ophiolites, island arc metavolcanics and minor ridges of metasediments. It is separated from Gabal Hafafit by NW-SE major thrust with NE dipping. The whole intrusion is located inside highly strained Nugrus shear zone which led to deform and mylonitize most rocks scattered in the area. The rocks are chronologically classified according to field relations and lithology into the following types:

3.1a-Gneisses and amphibolite

They are represented by hornblende, biotite and psammitic gneisses forming the major areas of Gabal Hafafit and the domal structures at the south-western areas of GMG (Fig. 2).

3.1b-Ophiolitic mélange

These rocks cover an area of about 90 km^2, and are composed of slivers and rock fragments of mountainous size that constitute of serpentinite fragments mounted in schists (talc-schist, beryliferous tremolite/actinolite schist, graphite schist and biotite schist) and cataclastic rocks. *The ultramafic rocks* are mainly composed of serpentinites that commonly weathered into sheared sub rounded boulder blocks varying in their sizes from few meters to mountainous block masses. The serpentinites are greenish grey to black and sometime have brownish grey colors and commonly occupy the upper horizons and show well developed mesh texture (Fig. 3a). Both types are frequently altered to buff-colored talc-carbonate rocks especially near the contact with the other rocks. *Talc schists* are located to the west of Wadi Gerf, forming relatively low land terrain 350 m above sea level and covering an area of about 1.5 km. These rocks are fine grained, grayish-white in color. They are intensively jointed and fractured, with major NE-SW and NW-SE trending joint sets that have steep angles of dip. *Tremolite-actinolite schists* form the most abundant rocks of the tectonic mélange, down thrusted under the ultramafic rocks. These rocks are highly tectonized , foliated with minor and major tight and open folds. *Graphite schists* have

a minor distribution and are only exposed in the form of thin bands (15- 40 cm thick) in the tectonic mélange exposed at the middle part of Wadi Gerf. The presence of graphite manifested their formation during regional metamorphism (greenschist facies) of organic sediments under relatively low P-T conditions. They are fine to medium grained, black-green to grayish black in color, highly foliated and are mainly composed of graphite, tremolite, quartz, calcite and chlorite. Measured foliations are of general WNW-ESE trend and southwest ward (25º) direction of dip.

3.1c-Island arc association

Island arc association is represented by chlorite schists and basic metavolcanics. Chlorite schists form black to grayish black long belts exposed at the eastern side of Wadi Nugrus (Fig. 2). They are almost consisting essentially of high corrugated big flakes of chlorite, and biotite. The meavolcanics are represented by older metavolcanics that expressed at the northern parts of the mapped area along Gabal Skait, and Hangalya (Fig. 2).

3.1d-The granitoid rocks

The granitoid rocks in the studied area are represented by two elongate belts flanked along the right and left sided of Wadi Nugrus. These two intrusions are namely Gabal El Magal El-Harami and Gabal Nugrus (Fig. 2). The two intrusions intrude the ophiolitic mélange and island arc association. The granitic rocks at Gabal Magal El-Harami, the target of the present study, are composed mainly of garnet bearing muscovite granite (GMG). The granites of Gabal Nugrus are syenogranite and alkali feldspar granite (Azer et al., 2024). The GMG is exposed at the western side of the regional mapped area (Fig. 2), where its exposure is large in size (>5.0 km^2) and emplaced along NW-SE trend, reached about 1-2 Km. in length and 250- 400 m. in width. The GMG intrudes the ophiolitic mélange (Fig. 3a) and commonly possesses sheared contact truncating the foliation of the schists at high angle. This granite is characterized by white color, fine to coarse-grained and occasionally pegmatitic. The variations in granite crystal sizes may be dueto influnced by the severe shearing prevailing within the area. The GMG is composed mainly of plagioclase, K-feldspar, quartz, muscovite and garnet which are visible in hand specimens.This leucogranite appears also as small off-shoots of boss-like bodies, as dyke-like bodies, and huge semicircular mass forming domal shapes (Fig. 3b). In some places, the leucogranite is highly deformed due to intensive tectonism (Fig. 3c). On the other hand, quartz veins are invaded into this granite and their surroundings. A NNW-SSE strike slip faults dislocate the muscovite granite pluton with common displacement. Some NNE-SSW basic dykes are cutting through the leucogranites. Some large white feldspar crystals and quartz grains were observed in pegmatitic variety, in addition to garnet grains seen in aplitic to coarse grained ones. Quartz veins are associated with the leucogranite with N-S trend cutting the country rocks. Reddish, brecciated and highly deformed quartz veins are associated with the leucogranite with N 50º E trend cutting the country rocks.

3.1e-Post granitic dykes

Most rock units of the studied area are cross-cut by basic dykes, quartz and pegmatitic veins. These dykes are NNW-SSE trending, fine-grained, differentially altered to clay minerals, and vary in thickness (Fig. 3d). The pegmatite veins are consisting of quartz, orthoclase, microcline, and micas. They commonly occur as ENE-WSW veins ranging from 50 cm to several meters in length, also they occur as pockets of flat lenses (10 m in length) at the margin and the core of the cataclastic rocks and ophiolitic mélange (Fig. 3e). Some of them contain heterogeneous masses of coarse-grained unidentified and red orthoclase, the latter being the most abundant constitute of feldspars. The

pegmatite veins are the main source of the rare metals, gold , magnetite and some sulfide minerals (Fig. 3f). Quartz veins have wide distributed in the studied rocks, the majority of quartz veins are barren, thin and short, they do not exceed 4.0 m length and 0.5 m thickness, thus they were not mapped. The quartz veins are cross cutting the foliation planes of ophiolitic mélange, trending NE and dipping 45˚/ NW.

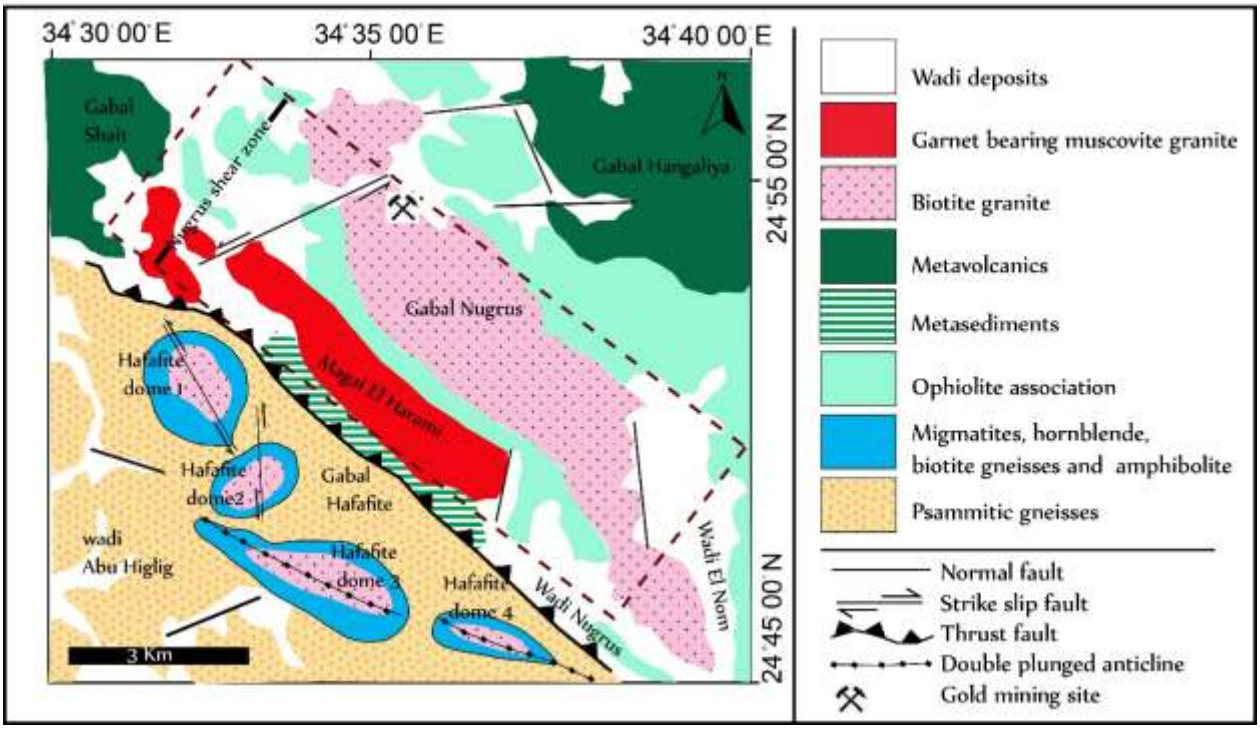

Fig.2. Geologic map of Magal El Harami and Nugrus granite intrusions at Wadi Nugrus. The domal structures at Gabal Hafafit are from El Fakarani et al., 2021.

3.2-Remote sensing data

The processed Landsat-8 false color composite band image (R:7, G:4, B:2) is useful in discrimination of major geology and main structural trends of the area beside the outline of the garnetiferous muscovite granites (Fig. 4a). In the processed false color composite band ratio image (R: 5/3, G: 5/1, B: 7/5) after Gad and Kusky 2006, the serpentinite masses have dark brown and green colors while the metavolcanics and amphibolite have violet color (Fig. 4 b). But this image failed to discriminate well between the granites varieties and the gneissose rocks in the area. The FCC Sultan ratios image (R: 5/7, G: 5/1, B: 5/4 * 3/4) after Sultan et al. (1986) reveals the serpentinites with bright red color owing to the band seven absorption by MgO– and OH– bearing minerals. Biotite granite of Gabal Nugrus has lemon color, while GMG and psammitic gneisses have light blue tone. The basic metavolcanics and amphibolites have dark blue signatures (Fig. 4c). The FCC image of minimum noise fraction (MNF) transform (Fig. 4d) delineates the serpentinite with light violet tone, biotite granites with light green tones, while dark green ridges represent exposures of biotite schists.

The principal component analysis technique can clarify the highest contrast in appearance of features from multispectral bands through combination of three PC images in RGB (Vincent 1997). In the present study, The combination of PC1, PC2, and PC3 differentiates the ophiolitic mélange with pale yellow and green colors, metavolcanics with blue and dark colors. Both

psammitic gneiss and granites are delineated with reddish and pink colors, however the resulted image failed to differentiate between granite types of the area (Fig. 5a). The RGB color combination (PC1, PC2, and PC4) effectively highlighted the ophiolitic mélange and biotite schist with yellow and green colors. The GMG has blue color, while Gabal Nugrus granite has pink signature, and metavolcanics have dark signature (Fig. 5b).

Fig. 3. Field photos showing: **a)** large mass of GMG intrudes the ophiolitic mélanges at Nugrus shear zone, photo looking NE, **b)** GMG appears a semicircular masses and domal shapes around Wadi Gerf, **c)** sharp contact between schists and GMG, photo looking NE, **d)** NNE-SSW to N-S basic dykes cut the GMG, photo looking NE, **e)** pegmatite veins cut the ophiolitic mélange of Wadi Nugrus, photo looking NE, **f)** ancient vertical excavation activities for rare metals (i.e. beryl) within GMG intrusion , photo looking NE.

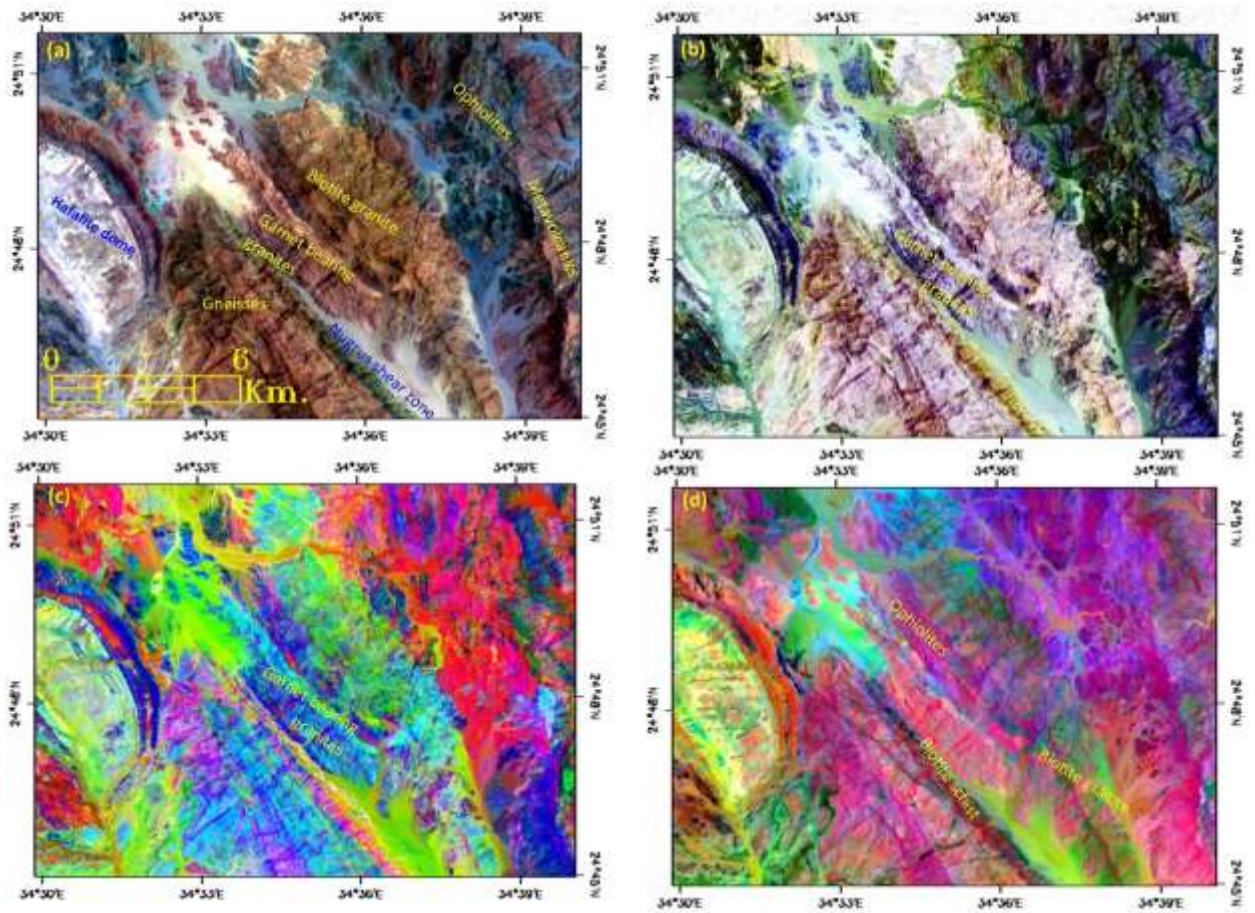

Fig. 4 . False color composite (FCC) images: **a)** FCC band image (R:7, G:4, B:2)., **b)** FCC band ratio image (R: 5/3, G: 5/1, B: 7/5) after Gad and Kusky 2006., **c)** FCC band ratio image (R: 5/7, G: 5/1, B: 5/4 * 3/4) after Sultan et al., 1986 **., d)** The minimum noise fraction (MNF) transform image (R: MNF3, G: MNF2, B: MNF6).

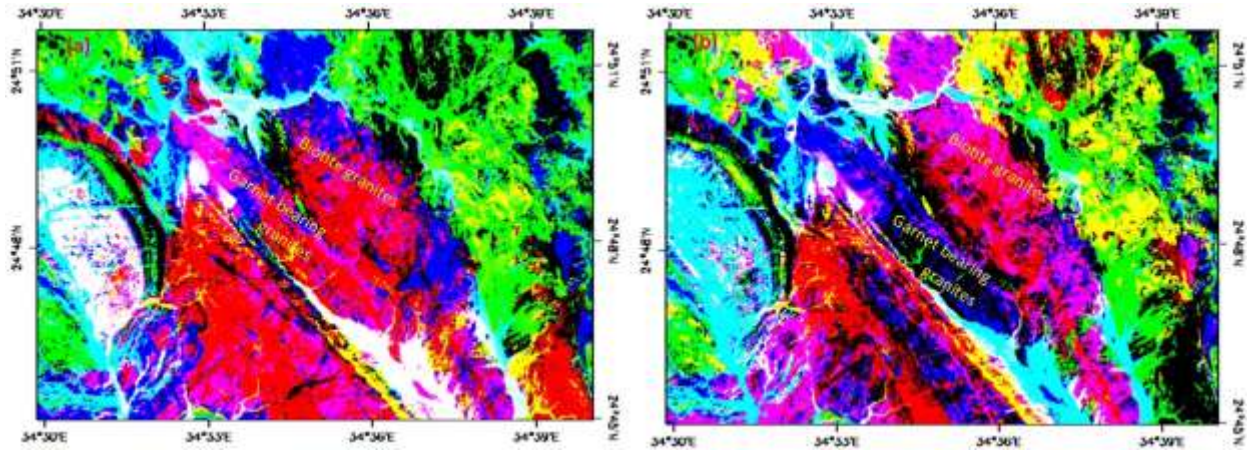

Fig. 5 . The principal component (PC) images : a) The RGB color combination of PC1, PC2, and PC3. , b) The RGB color combination of PC1, PC2, and PC4 respectively.

3.3-Petrography of GMG

The GMG is characterized by massive appearance of fine to coarse grained and occasionally pegmatitic size. It ranges in color from creamy to grayish pink and is composed mainly of plagioclase, potash feldspar, quartz, muscovite, and garnet with minor biotite. Epidote is secondary component, while zircon, tantalite, tourmaline, and opaque are accessory minerals. Plagioclase represents about 36.8% of the rock occurring as subhedral crystals of oligoclase with tabular forms (3.5mm length X 3.7mm width). It is characterized by albitic twinning and occasionally fractured and filled with opaques (Fig. 6a). Some crystals are partially epidotized, and others are traversed by muscovite along the fractures (Fig. 6b). Plagioclase crystals are occasionally zoned and are corroded along peripheries by microcline and may encloses amorphous allanite surrounded by pearly glassy zone (Figs. 6c, 6d). Microcline is the main potash feldspar and occurs as anhedral to subhedral crystals exhibiting its characteristic cross-hatched twining. It also occurs as subhedral crystals of microcline perthite (Fig. 6e). Quartz occupies about 33.5% in the leucogranites of GMG. It occurs as primary crystals often strained and characterized by undulose extinction. Muscovite is present in appreciable amounts (2.2%). Biotite occurs in minor amounts and partially chloritized. Garnet represents about 1.9% of the rock occurring as well-formed polygonal crystals (Fig. 6f), some crystals form coarse phenocrysts generally enclosing small nuclei of different minerals enclitic by radial fissures that may be related to radioactive effects (Fig. 6g). Zircon is rarely found as minute crystals enclosed in feldspars and exhibits abnormal interference colors referring to partial metamectization (Fig. 6h). It occurs as well-formed, zoned crystals included in quartz, and exhibits its characteristic interference colors of the third order. Epidote presents as secondary crystals enclosed in plagioclase, formed by a process of epidotization for plagioclase.

3.4-Mineralogy

This section is a brief description for mineralogy of columbite [$(Fe,Mn)(Nb,Ta)_2O_6$], tantalite [$(Fe,Mn)(Ta,Nb)_2O_6$], cassiterite [SnO_2], wolframite [$MnWO_4$] (Figs.7a -7d), ishikawaite [$(U,Fe,Y)(Nb,Ta)_2O_6$] , and euxenite-polycrase series [(Y, Ca, Ce, U, Th)(Nb, Ta, Ti)$_2O_6$- (Y, Ca, Ce, U, Th)(Ti, Nb, Ta)$_2O_6$]., in addition to beryl and tourmaline. Columbite occurs as black, flattened, prismatic and euhedral to subhedral crystals. Tantalite [$(Fe,Mn)(Ta,Nb)_2O_6$] are stained with iron oxide and are partially coated grains or all surface coated grains. Few grains form massive aggregates. Tantalite occurs as black to deep brown with metallic appearance, flattened, prismatic and euhedral to subhedral crystals. Wolframite occurs as thin lamina producing a lamellar structure. It occurs as brownish black to iron black and is mainly composed of W and Mn. Cassiterite is a brown, reddish or black in color, with compact massive structure and concentric patterns. The XRD pattern (Fig. 7b) shows the peaks at 2-theta 100, 81, 24, 5, 63, 8, 13, 17 and d-spacing 3.6, 2.6, 2.4, 1.7, 1.6, 1.4, 1.43. Euxenite has black color under the binocular microscope. The SEM spectrograph of euxenite shows that the mineral crystals are enriched in Al, Fe and Nb. Ishikawaite [$(U,Fe,Y)(Nb,Ta)_2O_6$] occurs as euhedral to subhedral crystals and ranges from 10 to 15 µm in sizes. There are two phases were distinguished, one is primary euhedral in and the other is replacing columbite mineral. Ishikawaite is confirmed by SEM spectrograph showing an enrichment of U, Fe and Mn within crystal lattice. *Tourmaline* has coarse grained well sided crystals (Fig. 7e). The SEM spectrograph of tourmaline shows that the mineral contain high values of Al, Mg, and Fe. Harraz and El Shaekawy 2001 ascribed the formation of tourmaline associated with quartz and pegmatites veins into B-metasomatism processes that may occur either during regional metamorphism or magmatism.

Fig. 6 . Photomicrographs showing: **a)** Euhedral crystal of plagioclase with pericline twining and partial alteration to epidote ., **b)** Fractured plagioclase filled with muscovite., **c)** Oscillatory zoned

crystal of plagioclase associating quartz and altered into zosite (Zo) **., d**) amorphous allanite in plagioclase., **e)** strained crystal of string perthite **., f)** Polygonal grains of garnet (Grt) scattered within the main constituents of GMG., **g)** A well formed phenocryst of garnet with inclusion of radioactive mineral., **h)** euhedral zircon crystal (Zr) with high birefringence within K-feldspars in GMG.

Zircon [$Zr(SiO_4)$] varies from short prismatic crystals to euhedral types with blunted edges. The investigated zircon are mostly luminous and generally show brilliant adamantine luster. Zircon crystals from GMG are generally colorless to pale yellow and honey colors, sometimes stained with iron oxides (Fig. 7e). The XRD pattern shows the peaks of zircon appear at 2-theta 45, 100, 8, 20, 14, 40 and d-spacing 4.42, 3.30, 2.63, 2.06, 1.9, 1.7. 6.2.d. *Garnet [$Fe_3Mn_3Al_2Si_3O_{12}$]* is commonly deep red to brownish black in colors. SEM data for the studied garnet proved almandine-spessartine rich types (Fig. 7f). *Apatite [$Ca_5(PO_4)_3(OH, F, Cl)$]* forms long prismatic euhedral crystals characterized by high phosphorus with P = 31.5, Ca = 66.3, but show low Fe content (Fig. 7g). *Fluorite (CaF_2)* exhibits colorless to pale green grains associated with iron oxides and contains some values of some rare earth elements (Fig. 7h). Generally, the investigated fluorite may occur either as disseminated grains or as small veinlets. The XRD peaks of fluorite appear at 2 theta 94, 100, 35 and d-spacing of 3.15, 1.93, 1.65.

3.5-Geochemistry

The studied samples of garnetiferous muscovite granite show wide variations in their silica contents (table 1). They have high contents of silica (72.3 – 76.6 wt.%), alumina, Al_2O_3 (12.92 – 15.75), and alkalis (T. alkalis 6.18 – 8.18), but they have low MnO, MgO and TiO_3 contents. The studied granites also posse high contents of normative orthoclase, albite and coundum with Or (20.28 – 32.34), Ab (22.94 – 43.34), and C (0.77 – 5.26). They also have high enrichment in Rb, Ba, Nb, Pb, Zn and Zr, but with depletion in Cu, Ni, Cr, V, and Sc. Plotting of the GMG samples on the CaO-Na_2O–K_2O diagram, after Archibald et al., (1981) (Fig. 8a), and on the diagram after Condie and Hunter (1976) (Fig. 8b), shows that the studied granites are mainly quartz monzonite. On the SiO_2 versus K_2O after Irvine & Baragar, 1971, and on Na_2O versus K_2O diagram after Alther et al., 2000 the studied granites have high K-calc alkaline nature (Fig. 8c, 8d)). Yuhara et al., (2003) used A/CNK against SiO_2 to differentiate between the peraluminous, metaluminous granites as well as S-type and I-type granites. The GMG samples are mainly peraluminous and are located in the S-type field (Figs.8e, 8f). Magmatic temperatures of GMG can be calculated from zircon saturation estimation after (Watson and Harrison, 1983). The calculated temperatures of zircon from GMG is (700-850^oC) (Fig. 9a). Plotting of the GMG samples on the R1-R2 diagram of de la Roche et al. (1980) majority of the samples are also located within the post orogenic range (Fig. 9b). On the Rb-Y-Nb diagram after (Pearce et al., 1984), the analysed samples are plotted near the triple point junction which reveals the post orogenic setting (Figs. 9c).

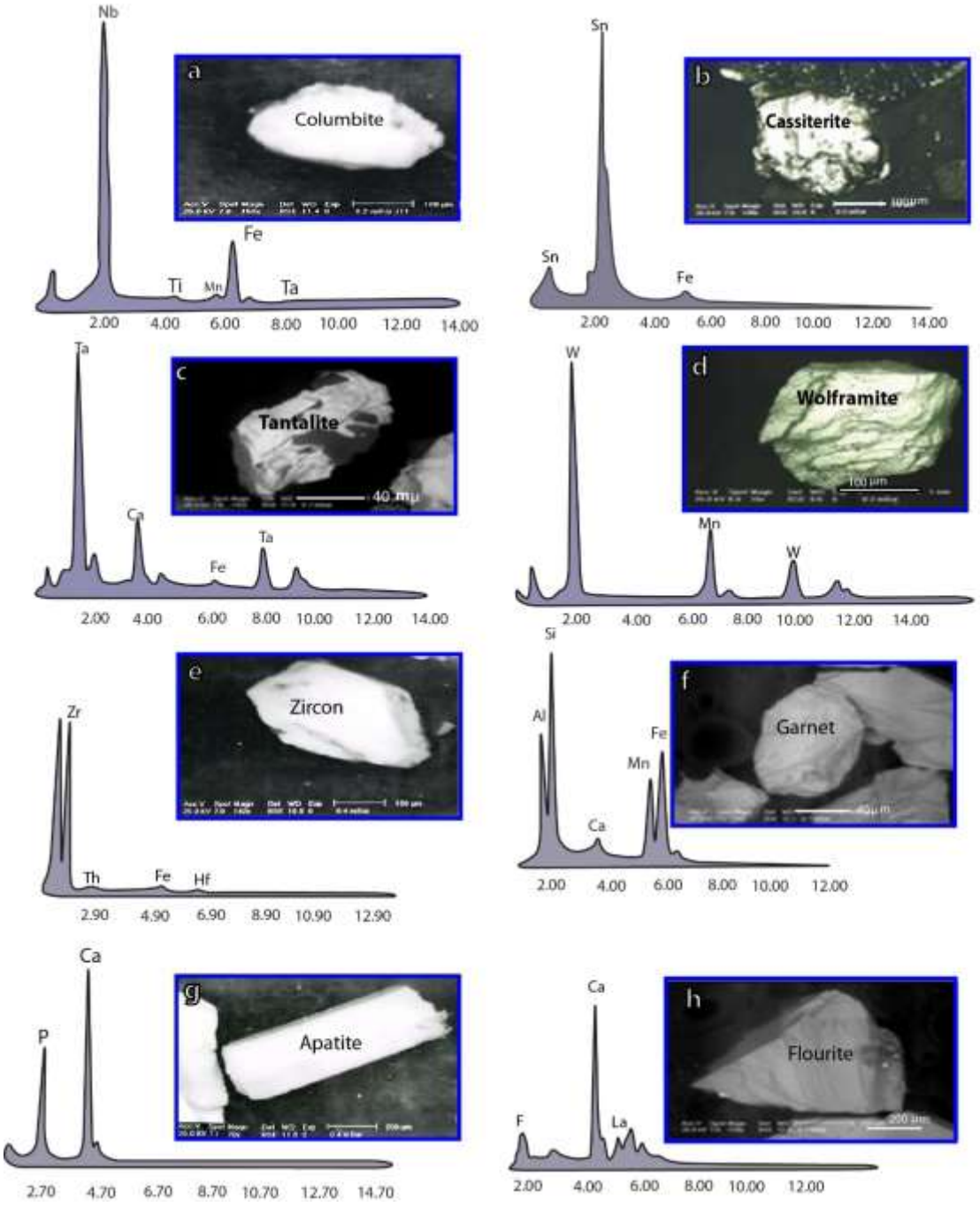

Fig. (7). (a) Scanning electron microprobe SEM spectrograph and back scattered images BSE of (a) Columbite (b) Cassiterite, (c) tantalite, (d) wolframite, (e) zircon, (f) garnet, g) apatite, h) fluorite.

Table 1: Chemical analyses of garnet bearing muscovite granite of Gabal El Harami

Sample No.	1	2	3	4	5	6	7	8	9	10	11	12	13	14	15	16	17	18	19	20	21
Major oxides (wt %)																					
SiO_2	74.29	75.71	73.57	73.46	73.91	76.6	76.08	73.07	73.75	72.7	73.51	72.8	76.54	72.27	74.3	75.69	73.47	75.22	76.75	75.36	74.75
TiO_2	0.31	0.05	0.3	0.28	0.25	0.11	0.2	0.21	0.2	0.18	0.22	0.19	0.05	0.02	0.29	0.07	0.26	0.02	0.01	0.02	0.01
Al_2O_3	14.03	13.36	14.46	14.76	14.26	12.98	12.92	14.76	14.45	14.07	14.65	14.43	14.52	15.75	14.05	13.41	14.55	13.74	13.19	14.85	14.65
Fe_2O_3	0.01	0.05	0.15	0.42	0.31	0.3	0.79	0.32	0.01	0.02	0.05	0.14	0.01	0.22	0.02	0.04	0.12	0.02	0.01	0.07	0.04
FeO	1.36	0.45	0.94	1.16	0.89	0.45	0.85	0.74	1.52	1.45	1.72	1.28	1.08	1.01	1.34	0.51	0.98	0.56	0.62	0.75	0.81
MnO	0.02	0.04	0.03	0.04	0.04	0.03	0.03	0.02	0.05	0.06	0.04	0.05	0.07	0.2	0.03	0.06	0.04	0.07	0.05	0.08	0.04
MgO	0.4	0.05	0.38	0.42	0.27	0.22	0.32	0.29	0.52	0.39	0.38	0.39	0.16	0.09	0.42	0.07	0.41	0.05	0.07	0.07	0.05
CaO	0.82	0.27	1.01	0.99	0.79	0.73	0.49	0.95	0.69	1.69	1.72	1.65	0.61	1.49	0.85	0.31	0.98	0.81	0.74	0.82	0.93
Na_2O	3.69	5.07	3.71	4.38	3.36	3.02	2.71	3.7	3.07	2.99	3.31	3.12	2.72	4.69	3.72	5.01	3.69	3.88	3.66	3.83	3.72
K_2O	4.63	3.71	4.55	3.51	5.45	4.91	5.24	4.88	3.82	3.96	3.49	3.81	3.46	3.4	4.62	3.68	4.39	3.83	4.36	3.95	4.09
P_2O_5	0.16	0.12	0.17	0.25	0.16	0.2	0.22	0.17	0.05	0.06	0.04	0.03	0.02	0.01	0.14	0.11	0.13	0.06	0.05	0.04	0.03
L.O.I.	0.83	0.52	0.86	0.79	0.69	0.55	0.6	0.65	1.15	2.39	0.58	1.48	1.41	0.59	0.86	0.52	0.81	0.85	0.49	0.46	0.62
Total	100.5	99.4	100.13	100.46	100.38	100.1	100.45	99.76	99.28	99.96	99.71	99.37	100.65	99.74	100.64	99.48	99.83	99.11	100	100.3	99.74

Table 1: continued

Sample No	1	2	3	4	5	6	7	8	9	10	11	12	13	14	15	16	17	18	19	20	21
CIPW Norms																					
Q	32.36	31.72	32.01	31.94	31.46	38.84	39.08	31.21	38.73	35.87	35.8	35.89	45.43	28.04	32.06	31.94	30.89	37.35	36.87	35.64	34.92
or	27.46	22.19	27.11	20.83	32.34	29.17	31.04	28.94	23.03	24.01	20.82	23.02	20.62	20.28	27.39	22	26.15	21.9	25.92	23.4	24.48
ab	31.27	43.34	31.59	37.14	28.49	25.64	22.94	31.35	26.44	25.9	28.22	26.94	23.16	39.98	31.51	42.79	33.71	33.44	31.09	32.42	31.82
an	3.14	0.64	4.05	3.46	2.99	2.46	1.14	3.73	3.19	8.24	8.38	8.19	2.93	7.4	3.4	0.9	4.13	3.74	3.4	3.84	4.49
C	1.79	0.77	1.96	2.49	1.73	1.79	2.36	2.02	4.18	1.95	2.39	2.27	5.26	1.67	1.67	0.86	1.78	2.11	1.2	2.86	2.49
Hy(MS)	1	0.13	0.96	1.05	0.68	0.55	0.8	0.73	1.32	1	0.96	1	0.4	0.23	1.05	0.18	1.03	0.13	0.18	0.18	0.13
Hy (FS)	2.02	0.78	1.17	1.4	1.04	0.45	0.63	0.79	2.59	2.52	2.85	2.05	2.03	2.03	2.02	0.91	1.35	1.13	1.21	1.44	1.53
mt(FF)	0.01	0.07	0.22	0.61	0.45	0.44	1.15	0.47	0.01	0.03	0.07	0.21	0.01	0.32	0.03	0.06	0.18	0.03	0.01	0.1	0.06
il(FT)	0.59	0.1	0.57	0.53	0.48	0.21	0.38	0.4	0.39	0.35	0.42	0.37	0.1	0.04	0.55	0.13	0.5	0.04	0.02	0.04	0.02
Ap(CP)	0.35	0.26	0.37	0.55	0.35	0.44	0.48	0.37	0.11	0.13	0.09	0.07	0.04	0.02	0.31	0.24	0.29	0.13	0.11	0.09	0.07

Table 1: continued

Trace elements (ppm)																					
Sample No	**1**	**2**	**3**	**4**	**5**	**6**	**7**	**8**	**9**	**10**	**11**	**12**	**13**	**14**	**15**	**16**	**17**	**18**	**19**	**20**	**21**
Rb	305	588	235	269	360	135	397	245	110	130	101	99	249	132	312	476	229	310	580	230	255
Ba	222	201	245	578	305	256	99	410	679	590	629	932	410	390	220	204	239	210	199	310	143
Pb	31	28	35	30	40	48	20	41	28	22	24	20	27	30	29	30	36	30	25	35	32
Sr	79	75	84	182	99	96	26	139	135	140	149	181	76	75	82	76	86	180	86	70	89
Y	18	8	17	10	15	16	35	16	17	14	20	16	9	19	17	9	16	19	20	19	18
Th	10	2	5	10	12	2	7	9	20	24	20	14	10	18	13	10	19	11	20	19	19
U	5	2	8	4	12	1	3	3	7	6	5	6	3	5	6	3	7	3	5	5	6
Zr	103	46	82	130	89	35	79	86	131	102	155	119	122	98	110	46	79	55	98	80	101
Nb	14	13	11	16	15	5	9	8	5	9	4	8	10	15	13	10	9	10	13	12	8
Zn	46	70	39	65	40	25	39	41	35	25	36	30	51	37	51	69	42	50	49	45	59
Cu	8	3	12	12	5	9	9	8	18	28	19	22	10	41	10	13	15	10	8	12	14
Ni	4	3	4	6	5	6	7	8	10	7	4	6	9	11	6	4	4	17	2	6	11
V	13	4	9	14	10	6	11	9	18	10	16	11	12	8	10	5	10	10	15	16	11
Cr	9	3	5	6	4	3	4	7	8	7	7	10	8	6	10	4	7	4	5	20	17
Ga	22	26	23	24	25	19	16	20	18	16	20	17	25	23	21	20	24	22	24	20	24
Cs	12	10	18	20	11	3	15	10	15	10	20	18	19	9	13	11	17	10	12	9	17

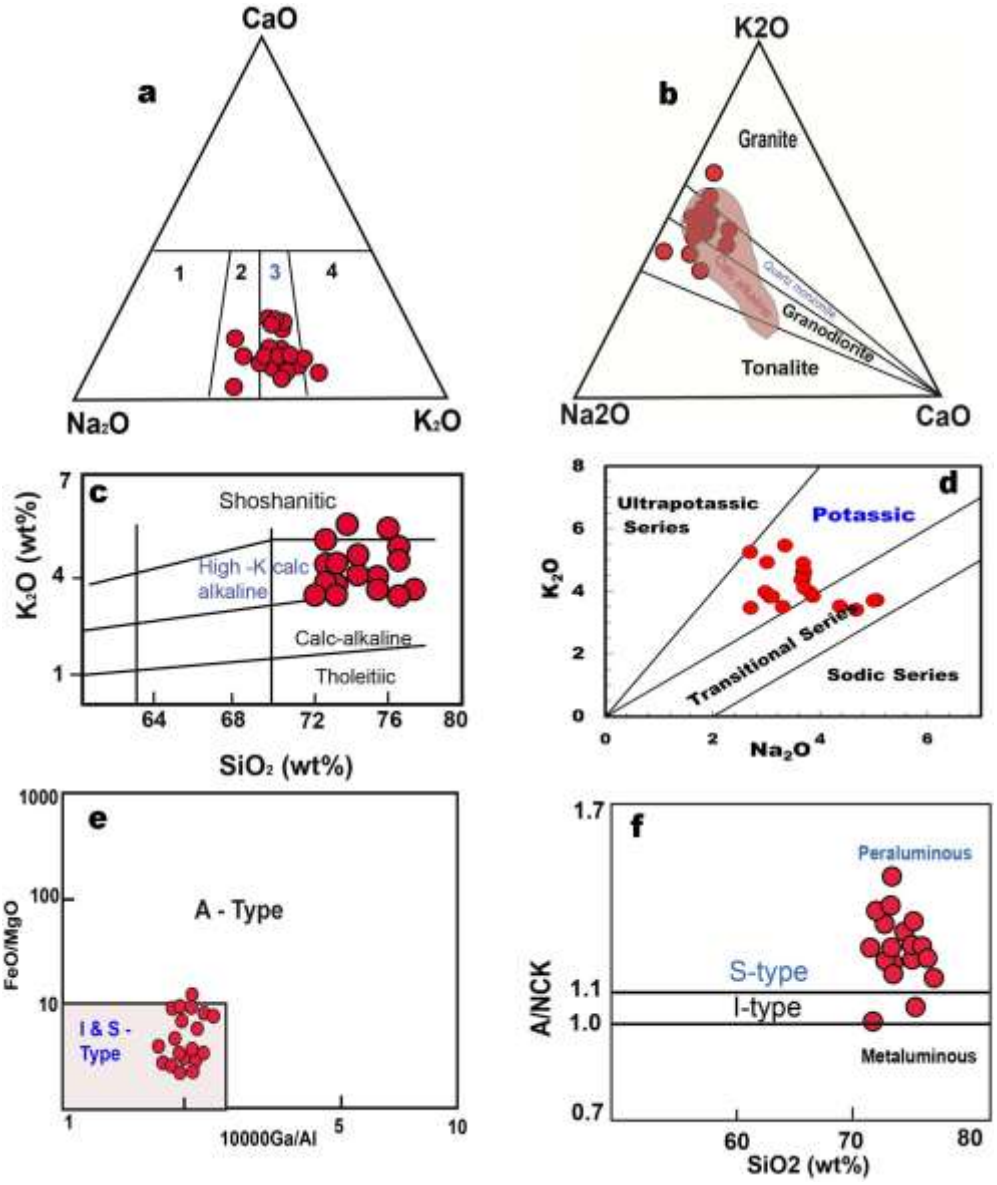

Fig. 8. Whole rock geochemical diagrams of **a)** CaO-Na_2O–K_2O ternary plot for granitic rocks after Archibald et al., (1981)., **b)** K_2O – Na_2O – CaO diagram after Condie and Hunter (1976), calc-alkaline field after Hunter (1979)., **c)** SiO_2 versus K_2O diagram after Peccerillo and Taylor (1976)., **d)** SiO_2 versus K_2O diagram after Alther et al., 2000., **e)** I & S, and A type granite discrimination diagram after Whalen et al. (1987)., **f)** A/CNK versus SiO_2 diagram after Yuhara et al., (2003).

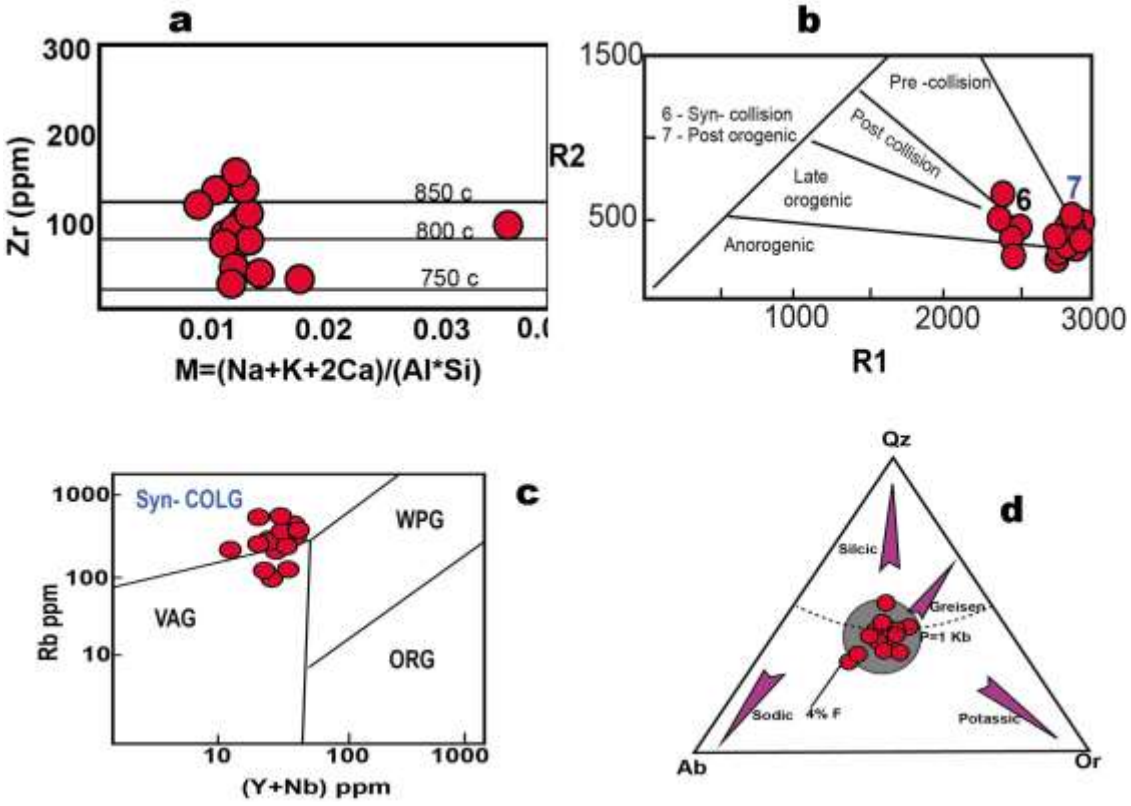

Fig. 9. Tectonic setting geochemical diagrams showing :a) Zircon against (Na+K+2Ca)/(Al × Si) represents the amount of zircon dissolved in granitoid melts at different temperatures after (Watson and Harrison, 1983), b): R1–R2 diagram for granitic rocks of after Batchelor and Bowden (1985)., c) Rb versus (Y + Nb) diagram for G. El Magal El Harami after Pearce et al., (1984)., d) Normative Quartz–Albite - Orthoclase ternary plot after Tuttle and Bowen (1958) and (Manning, 1981). The trends of granitic alteration types are from Stemprok (1979). Shaded area present the field of two mica leucogranites from the Himalaya after (Visona and Lombardo, 2002).

3.6. Petrogenesis of garnet bearing muscovite granite

Helz, (1976) mentioned that the highly peraluminous melts can be generated from the anatexis or remelting of metaluminous rich materials. Martin and Bowden (1981) suggested that S-type granites may present a pervasive alteration of any type of peraluminous or metaluminous granitoid. These are obtained through flowing of liquids and also alkali failure by vapor-phase conduction during late stages of magmatic crystallization. The GMG is peraluminous granites plot below the eutectic temperature and show a trend corresponding to crystallization in higher P_{H2O} range (0.5 – 3 Kb) (Fig. 9d). The 1 Kb P_{H2O} cotectic limit after (Tuttle and Bowen, 1958) and the movements path of the minima of magma with increasing fluorine after (Manning, 1981) are shown for comparison. The F-content increases in the sodic trend as illustrates by the A vector. Sylvester (1998) mentioned that, the S-type peraluminous granites that formed from clay-rich origin (plagioclase-poor) should have low CaO/Na_2O ratios generally less than (0.3), while that originated from clay-poor sources (plagioclase-rich) should have CaO/Na_2O ratios more than (0.3). Accordingly, the average CaO/Na_2O ratio from GMG is 0.23, this is combined with the fact that they plot with the field of two mica leucogranites from the Himalaya which formed though

dehydration melting of biotite-rich metapelites (Visona and Lombardo, 2002). The increase in F contents within the sodic trends, the existence of fluorite mineral, and the low K/Rb may indicate the existence of a volatile rich liquids in the main stage of GMG crystallization **(**Irber, 1999; Clarke, 1992). It is widely known that fluorine has great ability to form strong complexes with most HFSE and REE, these new compounds can raise the solubility of the less mobile elements within magma and may share in their economic enrichment (e.g. Audetat et al., 2000; Schönenberger et al., 2008; Agangi et al., 2010). Consequently, it is believed that the parental magma of GMG suffered an alteration with fluorine rich fluids that may form remarkable complexes causing the formation of garnet, and other HFSE such as tantalite, cassiterite and tourmaline.

3.7. Magma source and geotectonic environment

For many geologists, peraluminous magma is equivalent to S-type granites. In a recent study, Barbarin (1996) mentioned that some muscovite-bearing granitiods can be formed through extreme fractionations or local alteration of metaluminous melts, some moderately to highly peraluminous granites may be generated as a minor product of dominantly metaluminous granitiods suite. Collins, (1997) showed that the diversity and the cryptic characteristics of the muscovite granites can be demonstrated if the crystallized rocks were formerly a magmatic biotite granite that strongly affected by deformation producing cataclasis. The deformation may represents a younger resumption of the obliges that allow the muscovite bearing granites to generate, but the deformation may have happened at much lower temperature compare to that prevail during the older deformation, such process may helped to generate the metasomatic granites. Metasomatic fluids moving through the parent deformed biotite granite are believed to modify this rock to biotite-free muscovite granites. In this mechanism, the K-metasomatism may convert the relatively anorthite rich plagioclase into K- feldspars. More sodic plagioclase, myrmekite, and K, Al, and Si-metasomatism may transform biotite to muscovite and garnet minerals. Moreover, Brown and Solar (1998 a and b) and Sawyer et al. (1999) proposed dehydration melting model for the formation peraluminous granites. They showed that the relevance between high peraluminous granitic rocks and metasedimentary associations is explained to record syntectonic fluids influx within deforming crust. The domestic water fluxed melting being originate likely through muscovite dehydration at deeper crustal levels and then migrate upwards via structural pattern in melt, whereas larger masses of peraluminous granite demonstrate accumulation of the melts originated through muscovite dehydration melting at the deeper levels. Movement of granitic magma through the crust may be demonstrated by the synchronous deformation (Brown and Solar, 1999), while H_2O migration flux within the melt may help to support the prevalence of fissures to permit more effective motion of the highly viscous melts by exsolution of the vapor at the propagating fissures tip (encourage by the tendency in pressure at that site (Weinberg and Searle, 1999). The final result is granite rocks with high (H_2O) content formed at deeper levels moves to upper levels through the fractures. According to Sylvester (1998) the formation of peraluminous granites is usually interpreted as related either to crustal thickening connected with collision or to the period of extension which follows the collision. Crustal condensation occurs during collision mechanisms may lead to accumulation of metasedimentary and crustal rocks piles close to their melting temperature. The partial melting may be triggered by the addition of water, or by heat provided by mantle-derived magmas underplating the crust or injected into it (Barbarin 1996).

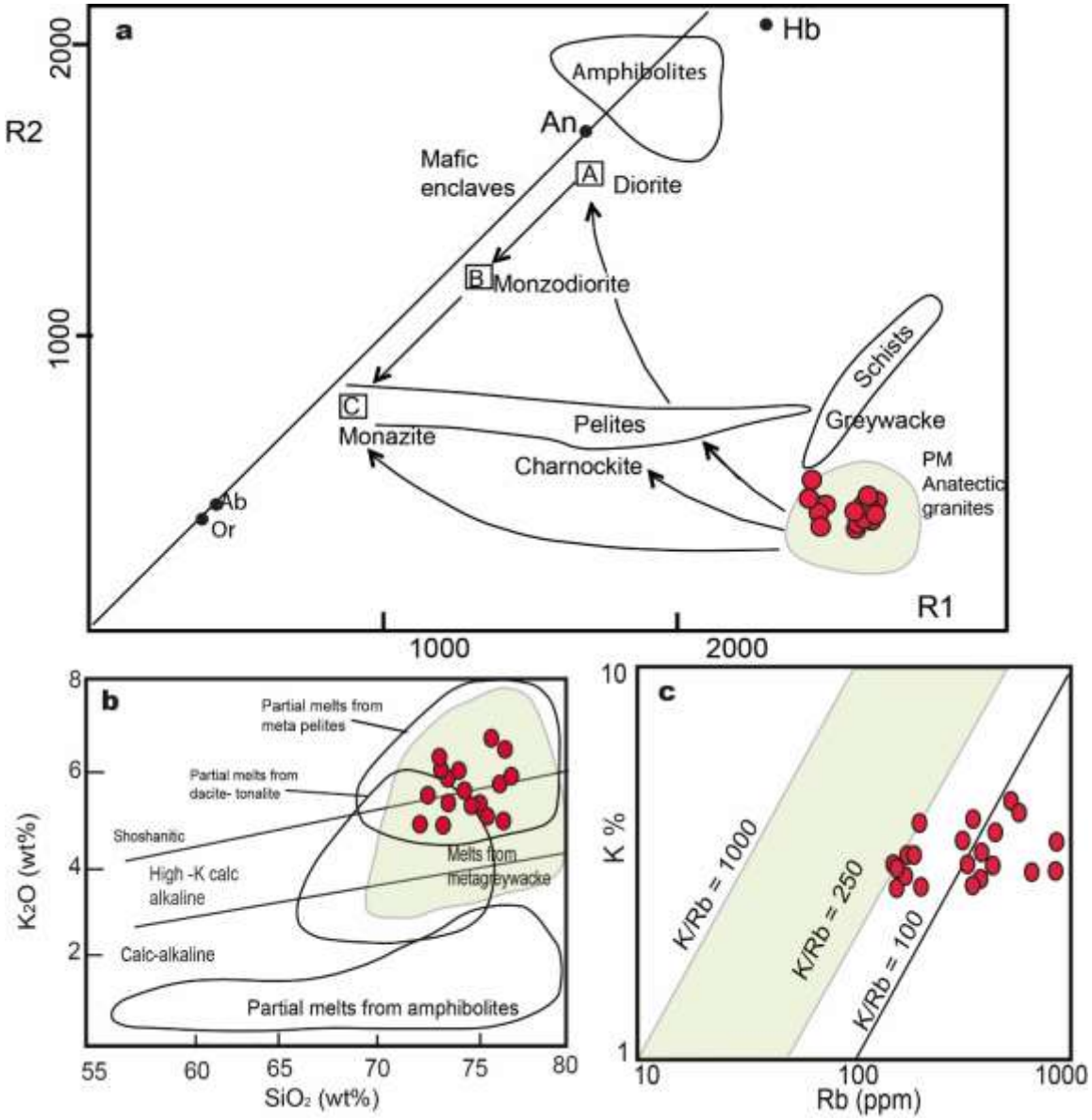

Fig. 10. **a)** R_1-R_2 geochemical diagram after (Batchelor and Bowden, 1985) showing partial melting vectors and metasedimentary and amphibolite sources. PM-A, PM-B and PM-C mark the modification in melt composition under progressive equilibrium partial melting. Hb = hornblende; An 50 = plagioclase (An 50)., **b)** plot of K_2O against SiO_2. Data for experimental melts from: Beard and Lofgren (1991)., **c)** the K % against Rb diagram after (Shaw 1968), the average crustal K/Rb ratio after Taylor (1965).

A possible magma source of the studied granitic rocks could be inferred from the R_1-R_2 binary plot after (Batchelor and Bowden, 1985) which discriminates between the different tectonic setting of granitic rocks using the multi-cationic parameters R1 and R2 of De La Roche et al. (1980). The R_1–R_2 diagram use the cationic/molecular values which express whole-rock chemistry as cationic parameters in terms of mineralogical component. It also shows partial melting vectors of metasedimentary and amphibolite sources. The partial melting PM (A, B, and C) represent the modification in melt configuration under progressive equilibrium. Plotting of (GMG) data on R_1–R_2 diagram (Fig. 10a) shows that the GMG granites are located within

anatectic granites which represents a products of crustal maturation by partial melting (Bartoli and Carvalho, 2021). Plotting of GMG samples on SiO_2 versus K_2O after Beard and Lofgren (1991), revealed that the studied granites were formed through re-melting of metagreywackes from the area (Fig. 10b). On the K-Rb binary plot (Fig. 10c), all the GMG samples plot around the crustal lines (K/Rb=250), and K/Rb=100 suggested by Taylor (1965) and far from the mantle limit (K/Rb=1,000) after Shaw (1968). This prove the high K affinity of the GMG, and their generation from lower crust source materials, and also suggested the high evolved granitic liquids of GMG.

4-Conclusion

The Gabal El magal El Harami garnet-bearing muscovite granite represents famous highly-fractionated granitic intrusion in the Wadi Nugrus, South Eastern Desert of Egypt. This intrusion consists essentially of quartz, akali-feldspars, albite and muscovite. The most important accessory phases comprise garnet, columbite, cassiterite, zircon, ilmenite, apatite, fluorite and monazite. The GMG has high potassium content, a peraluminous affinity, and was formed at post orogenic settings through partial melting of metapelites from lower crust under high pressure and temperature. The garnet crystals from GMG have spessartine-almandine composition. Fluorine-rich liquids may play an important role during the formation of garnet from GMG intrusion. At the late magmatic evolution of GMG, the hydrothermal overprint of F-rich solutions may led to formation of large complexes which may result in garnet and other HFSE enrichments.

References

Abu Elatta Abdallah Mahmoud, S., and Mansour, G.M. (2021). Petrogenesis, Geodynamics and Radioactivity of the Granitic Rocks of the Nugrus Weakness Zone, South Eastern esert, Egypt. Acta Geologica Sinica-English Edition, v. 95(4), p. 1183-1198.

Abu El-Rus, M. A. A., Mohamed, M. A., & Lindh, A. (2017). Mueilha rare metals granite, Eastern Desert of Egypt: An example of a magmatic-hydrothermal system in the Arabian-Nubian Shield. Lithos, 294, 362-382.

Agangi, A., Kamenetsky, V. S., and McPhie, J. (2010). The role of fluorine in the concentration and transport of lithophile trace elements in felsic magmas: insights from the Gawler Range Volcanics, South Australia. Chem Geol, 273: 314 – 325.

Ali, K. A., Moghazi, A. K. M., Maurice, A. E., Omar, S. A., Wang, Q., Wilde, S. A., ... & Stern, R. J. (2012). Composition, age, and origin of the~ 620 Ma Humr Akarim and Humrat Mukbid A-type granites: no evidence for pre-Neoproterozoic basement in the Eastern Desert, Egypt. International Journal of Earth Sciences, 101, 1705-1722.

Altherr, R., Holl, A., Hegner, E., Langer, C., Kreuzer, H. (2000). High potassium, calc-alkaline I-type plutonism in the European Variscides: northern Vosges (France) and northern Schwarzwald (Germany) Lithos 50:51–73.

Archibald, N. J., Bettenay, L. F., Bickle, M. J. and Groves, D. I. (1981). Evolution of Archean crust in the eastern Gold field province of Yilgaran Block, Western Australia. In Glover. J. E. and Groves, D. I. (eds); Archean geology. Geol. Soc. Australia, Special Publications, 7, p. 491 – 504.

Audetat, A., Gunther D., and Heinrich, C. A. (2000). Magmatic– hydrothermal evolution in a fractionating granite: a microchemical study of the Sn–W–F-mineralized Mole Granite (Australia). Gechim Cosmochim Acta, 19: 3373–3393.

Azer, M. K., Abuamarah, B. A., Srour, M. M., Wilde, S. A., & Gomaa, R. M. (2024). Mineralogy, geochemistry, and petrogenesis of post-collisional granites from the Arabian-Nubian Shield: Case study from the Gabal Nugrus area in the South Eastern Desert of Egypt. https://doi.org/10.1086/729331.

Barbarin, B. (1996). Genesis of the two main types of peralumious granitiods. Geolgy, Vol 24/4,P-295-298.

Bartoli, O. and Carvalho, B. B. (2021). Anatectic granites in their source region: a comparison between experiments, thermodynamic modelling and nanogranitoids. Lithos, 402, 106046.

Basta, F.F., Maurice, A.E., Bakhit, B.R., Azer, M.K., El-Sobky, A.F. (2017). Intrusive rocksof the Wadi Hamad Area, North EasternDesert, Egypt: Change of magmacomposition with maturity ofNeoproterozoic continental island arcand the role of collisional plutonism inthe differentiation of arc crust. Lithos.;288–289:248-263

Batchelor, R. A. and Bowden, P. (1985). Petrogenetic interpretation of granitoid rock series using multicationic parameters. Chem. Geol., Vol.48, P. 43 – 55.

Beard, J.S. and Lofgren, G.E., (1991). Dehydration melting and water-saturated melting of basaltic and andesitic greenstones and amphibolites at 1, 3, and 6.9 kb. Journal of Petrology 32 (2), 365–401.

Breiter, K., Ďurišová, J., & Dosbaba, M. (2020). Chemical signature of quartz from S-and A-type rare-metal granites–A summary. Ore Geology Reviews, 125, 103674.

Brown, M. and Solar, G. S. (1998a). Shear zones and melts: positive feedback in orogenic belts. Journal of Structural Geology **,** Vol .20, P.211-227.

Brown, M. and Solar, G. S. (1998b). Granite ascent and emplacement during continental deformation. Condergent orogens. Journal of structural geology, Vol.20, P.1365-1393.

Brown, M. and Solar, G. S. (1999). The mechanism of ascent and emplacement of granite magma during transpression: a syntectonic granite paradigm. Tectonophysics 309.

Clarke, D. B. (1992). Granitoids Rocks – Topics in the Earth Sciences,Series no.7. xi p. 283; London (Chapman and Hall).

Collins, L. G. (1997). Muscovite-garnet granites in the Mojave Desert: Relation to crustal structure of the cretaceous arc: Comment: Geology,Vol.25, P.187.

Condie, K. C. and Hunter, D. R. (1976). Trace element geochemistry of Archean granitic rocks from the Barberton region, South Africa. Earth Planet. Sci. Let., 29, P. 389 – 400.

De La Roche, H., Leterrier, J., Grandclaude, P. and Marchal, M. (1980). A classification of volcanic and plutonic rocks using R1 – R2 diagram and major element analyses; Its relationships with current nomenclature. Chem. Geol., Vol.29, P. 183 – 210.

El-Fakharani, A., Radwan, A., Hagag, W., Abdel-Rahman, E., & Younis, M. H. (2021). Structural and petrological re-assessed for the Najd-related shear zones along the Egyptian Eastern Desert. Arabian Journal of Geosciences, 14, 1-22.

El Hadek, H. H., Mohamed, M. A., El Habaak, G. H., Bishara, W. W., & Ali, K. A. (2016). Geochemical constraints on petrogenesis of Homrit Waggat rare metal granite, Egypt. Int J Geophys Geochem, 3(4), 33-48.

Emam, A., and Radwan, A. (2021). Geochemistry and petrogenesis of I-type granitoid rocks around Nasb-Zurar intrusion, West Wadi Allaqi, South Eastern Desert, Egypt. Arabian Journal of Geosciences, 14, 1-17.

Emam, A., Zoheir, B., Radwan, A. M., Lehmann, B., Zhang, R., Fawzy, S., & Nolte, N. (2018). Petrogenesis and evolution of the Nuweibi rare-metal granite, Central Eastern Desert, Egypt. Arabian Journal of Geosciences, 11, 1-15.

Fowler, A., and Osman, A. F. (2009). The Sha'it–Nugrus shear zone separating Central and South Eastern Deserts, Egypt: a post-arc collision low-angle normal ductile shear zone. Journal of African Earth Sciences, 53(1-2), 16-32.

Gad, S., and Kusky, T. (2006). Lithological mapping in the Eastern Desert of Egypt, the Barramiya area, using Landsat thematic mapper (TM). Journal of African Earth Sciences, 44(2), 196-202.

Gharib, M.E., Saleh, G.M, Attia, G.M, Abu Zeid, E.K., and Mahmoud, G.B. (2011). Mineralogical and Geochemical studies on the leucogranites at Gabal Magal El Harami area, south Eastern Desert, Egypt. Egyptian Journal of Geology, v. 55, p. 247-266.

Govindaraju, K. (1984). Compilation of working values and sample description for 170 international reference samples of mainly silicate rocks and minerals. Geostandards Newsletter, Special Issue No. 8.

Harraz, H. Z., & El-Sharkawy, M. F. (2001). Origin of tourmaline in the metamorphosed Sikait pelitic belt, south Eastern Desert, Egypt. Journal of African Earth Sciences, 33(2), 391-416

Hassan, M. A. and Hashad, A. H. (1990). Precambrian of Egypt. In: Said, R. (ed.). The geology of Egypt. Balkema, Rotterdam / Brookfield.

Helz, R. T. (1976). Phase relations of basalts in their melting range at $P_{(H2O)}$ = 25 kb. 2 Melt compositions. J. of Petrology,Vol. 17, p. 139-193.

Hunter, D. R., (1979). The role of tonalitic and trondhjemitic rocks in the crustal development of Swaziland and the Eastern Transvaal, South Africa. In: Barker, F. (ed.): Trondhjemites, dacites and related rocks. Elsevier, Amsterdam, P. 303 – 322.

Irber, W. (1999). The lanthanide tetrad effect and its correlation with K/Rb, Eu/Eu*, Sr/Eu, Y/Ho, and Zr/Hf of evolving peraluminous granite suites. Geochim Cosmochim Acta, 63: 489 - 508.

Irvine, T. N., & Baragar, W. R. A. F. (1971). A guide to the chemical classification of the common volcanic rocks. Canadian journal of earth sciences, 8(5), 523-548.

Kroner, A., Kruger, J. and Rashwan, A.A. (1994). Age and tectonic setting of granitoid gneisses in the Eastern Desert of Egypt and Southwest Sinai, Geol. Rundesch ,Vol. 83, P. 502-513

Lehmann, B., Zoheir, B. A., Neymark, L. A., Zeh, A., Emam, A., Radwan, A. M., ... & Moscati, R. J. (2020). Monazite and cassiterite UPb dating of the Abu Dabbab rare-metal granite, Egypt: Late Cryogenian metalliferous granite magmatism in the Arabian-Nubian Shield. Gondwana Research, 84, 71-80.

Liégeois, J-P, and Stern, R. J. (2010). Sr-Nd isotopes and geochemistry ofgranite-gneiss complexes from the Meatiq and Hafafit domes,Eastern Desert, Egypt: no evidence for pre-Neoproterozoic crust.J Afr Earth Sc 57:31–40.

Manning, D. A. C. (1981). The effect of fluorine on liquidus phase relationships in the system Qz – Ab – Or with excess water at 1 kb. Contrib. Mineral. Petrol., Vol. 76, P. 206 – 215.

Martin, R. F., and Bowden, P. (1981). Peraluminous granites produced by rock-fluid interaction in the Ririwai nonorogenic ring-complex, Nigeria: mineralogical evidence. Can Mineral, 19, 65-82.

Moghazi, A. M. (1999). Magma source and evolution of late Neoproterozoic granitoids in the Gabal El Urf area, Eastern Desert, Egypt: geochemical and Sr–Nd isotopic constraints. Geol. Mag. 136: 285- 300

Moghazi, A, M., Iaccheri, L.M., Bakhsh, B.A., Kotov, A.B., Ali, K.A. (2015). Sources of rare-metal-bearing A-type granites from Jabel Sayed complex, Northern Arabian Shield, Saudi Arabia. J Asian Earth Sci 107:244–258**.**

Pearce, J. A., Harris, N. B. W. and Tindle, A. G. (1984). Trace element discrimination diagrams for the tectonic interpretation of granitic rocks. J. Petrol., Vol.25, P. 956 – 983.

Peccerillo, A. and Taylor, S.R., (1976). Geochemistry of Eocene Calc-Alkaline Volcanic Rocks from the Kastamonu Area, Northern Turkey. Contributions to Mineralogy and Petrology, 58, 63-81.

Sawyer, E. W., Dombrowski, C., & Collins, W. J. (1999). Movement of melt during synchronous regional deformation and granulite-facies anatexis, an example from the Wuluma Hills, central Australia. Geological Society, London, Special Publications, 168(1), 221-237.

Schönenberger, J., Köhler, J., and Markl, G. (2008). REE systematics of fluorides, calcite and siderite in peralkaline plutonic rocks from the Gardar Province, South Greenland. Chem Geol, 247: 16 - 35.

Shapiro, L. and Brannock, W. W. (1962). Rapid analysis of silicate, carbonate and phosphate rocks, U. S. Geol. Surv. Bull, 114 A, 56 P.

Shaw, D.M. (1968). A review of K-Rb fractionation trends by covariance analyses. Geochim Cosmochim Acta 32:573–601.

Stemprok, M. (1979). Mineralized granites and their origin. Episodes Journal of International Geoscience, 2(3), 20-24.

Stern, R.J. (1994). Arc assembly and continental collision in theNeoproterozoic East African orogen: implications for theconsolidation of Gondwanaland. Annu Rev Earth Planet Sci22:319–351

Stern, R.J., and Hedge, C.E. (1985). Geochronologic and isotopic constraintson late Precambrian crustal evolution in the Eastern Desert ofEgypt. Am J Sci 285:97–172**.**

Sultan, M., Arvidson, R.E., Sturchio, N.C. (1986). Mapping ofserpentinites in the E. Desert of Egypt using Landsat Thematic Mapper data. Geology 14, 995–999**.**

Sylvester, P. J. (1998). Post-collisional strongly peraluminous granites. Lithos 45, 29-44.

Taylor, S.R. (1965). The application of trace element data problems in petrology. In: Ahrens LH, Press F, Runcor SR, Urey HC (eds). Physical and chemical of the earth, pp 133-213.

Tuttle, O. F. and Bowen, N. L. (1958). Origin of granite in the light of experimental studies in the system $NaAlSi_3O_8$-$KAlSi_3O_8$-SiO_2-H_2O. Geol. Soc. Am. Em., 74, 153 P.

Vincent, R.K. (1997). Fundamentals of geological and environmental remote sensing (vol. 366). Prentice Hall, Upper Saddle River, NJ

Visona, D., Lombardo, B. (2002). Tow- mica and tourmaline leucogranites from the everest-makalu region (Nepal- tibet). Himalayan leucogranites genesis by isobaric heating [J]. Lithos 62, 125-150.

Watson, E. and Harrison, T. M. (1983). Zircon saturation revisited: temperature and composition effects in a variety of crustal magma types. J. Earth Planet Sci. Lett., Vol. 64, P. 295 – 304.

Weinberg, R. F., and Searle, M. P. (1999). Volatile-assisted intrusion and autometasomatism of leucogranites in the Khumbu Himalaya, Nepal. Journal of Geology, Vol .107,P. 27-48.

Whalen, J.B., Currie, K.L., Chappell, B.W. (1987). A-type granites: geochemical characteristics, discrimination and petrogenesis. Contrib Mineral Petrol 95:407–419

Yuhara, M., Miyazaki, T., and Kagami, H. (2003). Rb-Sr and K-Ar gheochemistry and petrogenesis of the Aji granite in the eastern Sanuki district, Ryoke Belt, South West Japan. J. Min. and Petr. Sci., Vol.98, P. 19-30.

Zoheir, B., Lehmann, B., Emam, A., Radwan, A., Zhang, R., Bain, W. M., M Steele-MacInnis, & Nolte, N. (2020). Extreme fractionation and magmatic–hydrothermal transition in the formation of the Abu Dabbab rare-metal granite, Eastern Desert, Egypt. Lithos, 352, 105329.